CORA Cork Open Research Archive
Cartlann Taighde Oscailte Chorcaí

Title	Magnetic performances and switching behavior of Co-rich CoPtP micro-magnets for applications in magnetic MEMS
Authors	Mallick, Dhiman;Paul, Kankana;Maity, Tuhin;Roy, Saibal
Publication date	2019-01-08
Original Citation	Mallick, D., Paul, K., Maity, T. and Roy, S. (2019) 'Magnetic performances and switching behavior of Co-rich CoPtP micro-magnets for applications in magnetic MEMS', Journal of Applied Physics, 125(2), 023902 (14 pp). doi: 10.1063/1.5063860
Type of publication	Article (peer-reviewed)
Link to publisher's version	https://aip.scitation.org/doi/abs/10.1063/1.5063860 - 10.1063/1.5063860
Rights	© 2019 the authors. Published under license by AIP Publishing. This article may be downloaded for personal use only. Any other use requires prior permission of the author and AIP Publishing. The following article appeared in Journal of Applied Physics and may be found at https://doi.org/10.1063/1.5063860
Download date	2026-11-01 21:18:10
Item downloaded from	https://hdl.handle.net/10468/7756



UCC
University College Cork, Ireland
Coláiste na hOllscoile Corcaigh

Journal of Applied Physics

Magnetic performances and switching behavior of Co-rich CoPtP micro-magnets for applications in magnetic MEMS

Cite as: J. Appl. Phys. **125**, 023902 (2019); https://doi.org/10.1063/1.5063860
Submitted: 02 October 2018 . Accepted: 21 November 2018 . Published Online: 08 January 2019

Dhiman Mallick, Kankana Paul, Tuhin Maity, and Saibal Roy

COLLECTIONS

This paper was selected as Featured

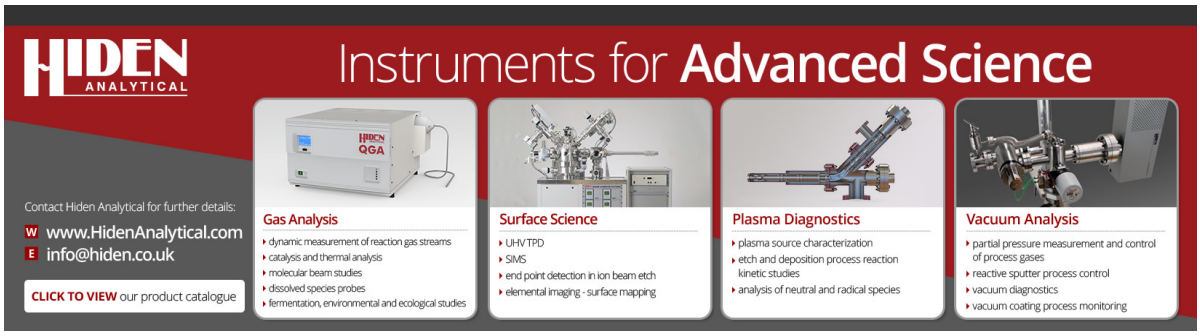
View Online Export Citation CrossMark

ARTICLES YOU MAY BE INTERESTED IN

New deposition process and design for CoPtP micromagnets
Scilight **2019**, 020001 (2019); https://doi.org/10.1063/1.5086179

Investigation and modeling of optics damage in high-power laser systems caused by light backscattered in plasma at the target
Journal of Applied Physics **125**, 033101 (2019); https://doi.org/10.1063/1.5070066

Steady-state and transient behavior in dynamic atomic force microscopy
Journal of Applied Physics **125**, 044301 (2019); https://doi.org/10.1063/1.5078954



© 2018 Author(s).

Journal of Applied Physics ARTICLE scitation.org/journal/jap

Magnetic performances and switching behavior of Co-rich CoPtP micro-magnets for applications in magnetic MEMS

Cite as: J. Appl. Phys. **125**, 023902 (2019); doi: 10.1063/1.5063860
Submitted: 2 October 2018 · Accepted: 21 November 2018 ·
Published Online: 8 January 2019

View Online Export Citation CrossMark

Dhiman Mallick,[1] Kankana Paul,[1] Tuhin Maity,[1] and Saibal Roy[1,2,a)]

AFFILIATIONS

[1]Micro-Nano-System Center, Tyndall National Institute, Cork, Ireland
[2]Department of Physics, University College Cork, Cork, Ireland

[a)]Email: saibal.roy@tyndall.ie

ABSTRACT

In this paper, the magnetic properties of Co-rich CoPtP films electrodeposited using an optimized Pulse Reverse (PR) technique are investigated for magnetic MEMS applications. By using a combination of forward and reverse pulses with optimized duty cycles during deposition and suitable bath chemistry, the film stress is reduced significantly, which results in smooth, crack-free films of thickness up to 26 μm. The deposited film of thickness ~3 μm shows a coercivity of 268 kA/m, a remanence of 0.4 T, and a maximum energy product of 35 kJ/m^3 in the out-of-plane direction. The variation in the hard-magnetic properties of the films for changing the film thickness is analyzed in terms of the composition, crystalline structure, and grain size. As the thickness is increased from 0.9 μm to 26 μm, the in-plane coercivity reduces by 17% due to an increase of the grain size and the Co content in the alloy structure. The in-plane squareness factor increases by 1.5 times as the thickness is increased over the above-mentioned range, which results in an enhancement of the in-plane remanence value. The magnetization reversal behavior of the deposited films indicates that the nature of magnetic interaction is significantly influenced by the thickness of the films, where the dipolar interaction for the thinner films changes to exchange coupling at higher thickness due to the increase of the grain size. Finally, an innovative design strategy to integrate CoPtP in magnetic MEMS devices by micro-patterning is proposed and analyzed using the finite element method. The demagnetization fields of the magnetic elements are minimized through optimized micro-patterned structures which improve the viability of PR deposited CoPtP micro-magnets having suitable nano-grains in potential MEMS based applications.

Published under license by AIP Publishing. https://doi.org/10.1063/1.5063860

I. INTRODUCTION

The recent development in the hard-ferromagnetic (FM) alloys and compounds, also referred to as permanent magnets, is driven by the potential applications of thin films in high-density recording media[1,2] and of thick films in micro/nano-electromechanical systems (M/NEMS).[3,4] While the market of hard magnets is dominated by sintered, bulk NdFeB (maximum energy product $BH_{max} = 450$ kJ/m^3) discrete magnets,[5] the CMOS compatible integration remains a crucial challenge due to high temperature processing. Therefore, a number of fabrication techniques including powder-based fabrication methods[6,7] (dry-packing, screen printing, etc.) and conventional thin film deposition techniques such as sputtering,[8–10] pulse laser deposition (PLD),[11,12] and electrochemical deposition[13–17] have emerged over the years depending on the application requirements. Among the various techniques currently being exploited for device integration, electrochemical deposition is an attractive choice due to its low cost and a relatively high deposition rate at CMOS permissible temperature.

Sputtered rare-earth compounds like NdFeB and SmCo, among the best performing micro-magnets, are often hindered by the requirements for the specialized deposition system and high annealing temperatures. The growth of the face-centered tetragonal (fct) $L1_0$ structure in transition

metal alloys Co/Fe-Pt with equi-atomic ratios has received extensive attention due to the high uniaxial magneto-crystalline anisotropy ($K_1 = 6.6\ MJ/m^3$). The ordered $L1_0$ structure of equiatomic Co/Fe-Pt films with varying thicknesses has been deposited by sputtering,[8–10] PLD,[11,12] and electrodeposition[13–15] techniques. However, the phase transformation and the desired hard magnetic properties are obtained at either elevated substrate temperature during deposition (sputtering) or by high temperature, post-deposition annealing (electrodeposition).

On the other hand, Co rich Co-Pt alloys with an atomic ratio of 80:20 exhibit good hard magnetic properties without any requirement of the high temperature annealing step, making them a good candidate for CMOS/MEMS integration. Such hard-magnetic properties can be availed in the as-deposited state due to the high magnetic anisotropy induced by incorporating Pt in the hexagonal closed-packed (hcp) phase of Co and phosphorous-segregated grain boundaries. The properties of $Co_{80}Pt_{20}$ and $Co_{80}Pt_{20}P$ were compared by Callegaro *et al.*,[18] where it was reported that the addition of phosphorus to the electrolyte for CoPt deposition induces P co-deposition and improves films' hard magnetic properties. The addition of P improved the coercivity (H_C) of CoPt films from 220 kA/m to 440 kA/m, along with an increased squareness of 0.7. Vieux-Rochaz *et al.*[19] reported that in-plane magnetization with coercivities as high as 220 kA/m can be reached for patterned layers of CoPtP electrodeposited using an acidic bath for micromagnetic sensor applications. Ramulu *et al.*[20] recently reported the three-electrode potentiostatic electrochemical synthesis and the characterization of one dimensional hard magnetic CoPtP nanowires. They deposited nanowires into a nano-porous track-etched polycarbonate membrane with a nominal pore diameter of 50 nm and a thickness around 6–9 μm. The coercivities were measured to be 140 kA/m and 100 kA/m along parallel and perpendicular directions to the nanowire axis, respectively. The phosphorous segregation in the grain boundaries is enhanced by Wang and Arnold[21] using textured seed layers, e.g., Cu (111) on Si (110), that provides a template lattice for the desired crystalline structure. They demonstrated 8-μm-thick patterned films with an energy product of $69\ kJ/m^3$. In many cases, however, the deposition is restricted to 1-2 μm thickness as the magnetic properties deteriorate significantly with thickness and as the film stress increases resulting in micro-cracks in the structural morphology. Our group previously reported[22] that a combination of pulse-reverse (PR) plating with the addition of stress-relieving additives to the bath of CoPtP can considerably reduce the film stress. However, the formation of free poly-ammine in the electrolytic bath from the Pt-salt not only increases the stress in the electrodeposits but also reduces the chemical stability of the bath significantly.[23] Thus, a significant drop of magnetic properties with thickness and inhomogeneous growth due to instability of the electrolytic bath remained a challenge.

In this work, we have deposited homogeneous, stress free films of Co-rich CoPtP by optimized PR electrodeposition conditions and bath chemistry. A detailed study of microstructural evolution and magnetic properties of PR electrodeposited CoPtP films with varying thickness values is presented. Iso-thermal remanence (IRM) and dc demagnetization (DCD) measurements of CoPtP films are performed in order to study the magnetic domain switching behavior. Finally, an innovative design scheme to integrate the developed CoPtP magnetic material as a source of magnetic field in micro-scale MEMS devices is extensively analyzed using the finite element method (FEM).

II. EXPERIMENTAL METHODS

Co-rich CoPtP films are electrochemically deposited using an electrolytic bath, which consists of 0.1M cobalt sulfamate, 0.01M diammine-dinitro-platinum (Platinum-P-salt), 0.1M sodium hypophosphite, 0.1M dibasic ammonium citrate, 0.1M sulfamic acid, 0.1M glycine, and 0.25M saccharin.[21,22,24–26] Dibasic ammonium citrate acts as the complexing agent to bring the reduction potentials of cobalt and platinum close together. Glycine reduces the surface tension between the electrolyte and the working electrode, whereas saccharin is added in the electrochemical bath as a stress-relieving additive. Due to instability of the Platinum-P-salt, the electrolytic bath is often not sustained for a long time (more than few days) as solid precipitation occurs. To prevent this, sulfamic acid is added which forms diammine platinum disulfamate and restricts the formation of free poly-ammine in the bath.[23–26] This procedure stabilizes the platinum compound and increases the current efficiency significantly. The pH of the solution is monitored during the deposition process and adjusted to 8 by adding a small amount of NaOH. A piece of cobalt is used as the anode and silicon pieces ($1\ cm^2$ area) with sputtered Cu/Ti (200/20 nm) seed layers are used as the cathode. The electrochemical deposition is carried out at room temperature in a CH instrument CHI660C workstation. The deposition of platinum produces hydrogen evolution reaction which creates bubbles near the cathode surface causing non-uniformity in the deposition. To avoid this, the cathode is removed occasionally during the deposition and the bubbles are cleared to maintain a uniform deposition process.

The micro-structure and elemental characterization of the deposited films are performed using Quanta FEI 650 Scanning Electron Microscope—Energy Dispersive X-ray Spectroscopy (SEM-EDS) analysis. The 3D surface topology analyses of the films are performed using the tapping mode in Keysight 9500 Atomic Force Microscopy (AFM). Further microstructural analysis of the deposited samples is carried out using Jeol 2100 High-Resolution Transmission Electron Microscopy (HR-TEM) in conjunction with selected-area electron diffraction (SAED). The X-Ray diffraction (XRD) patterns are characterized in a Panalytical X'Pert Pro MRD with Cu Kα radiation (40 kV, 50 mA) at a wavelength of 1.54 nm for crystalline phase analysis. The magnetic measurements of the deposited films are carried out in Quantum Design SQUID magnetometer (MPMS-XL5) for an applied field up to 5 T.

Published under license by AIP Publishing.

III. RESULTS AND DISCUSSIONS

A. Pulse reverse electrodeposition of Co-rich CoPtP films

Three electrode cyclic voltammetry (CV) analysis is performed initially to estimate the deposition current density. Based on that, the first film is deposited using a conventional direct current (DC) plating technique at a current density of 20 mA/cm^2, which results in a composition of 77.6% Co, 21.7% Pt, and 0.7% P. The surface morphology of the deposited film is shown in Fig. 1(a). The DC plated film is full of micro-cracks even though the stress relieving agent, saccharin, is added to the bath. It is to be noted that even a highly polished silicon wafer has nano-scale surface roughness, creating an uneven Nernst diffusion layer. As a result, a smaller diffusion length from the peak and a larger diffusion length from the valley are obtained for the uneven surface for depositing ions. This gives rise to a relatively higher metal ion concentration, and hence a greater deposition rate, at the peaks than the valleys. This preferential growth of the metal alloy leads to the non-uniformity of the entire film and, as a result, it is stressed.

To avoid this effect, a second film is electroplated using the PR Plating technique[27] with a current waveform, consisting of optimized forward and reverse current densities of 20 mA/cm^2 (20 ms) and 10 mA/cm^2 (0.5 ms), respectively; with intermediate off times of 0.5 ms. The complete cycle is repeated for the entire deposition duration. Several trials of reverse current durations and magnitudes have been used before optimizing the above-mentioned values. Increasing the reverse current duration or magnitude significantly results in stripping of the material rather than depositing. Decreasing the same affects the film stress considerably. The forward duty cycle (D_f) for the forward current and the reverse duty cycle (D_r) for the reverse current are given by

$$D_f = \frac{t_f}{T} \quad \text{and} \quad D_r = \frac{t_r}{T}, \tag{1}$$

where $T = t_f + t_r + 2t_o$ is the length of the entire one cycle, within which t_f is the forward cycle time, t_r is the reverse cycle time, and t_o is the off time. The film composition is found to be 79.6% Co, 19.2% Pt, and 1.2% P using EDS analysis. The nano-scale asperities from the surface of the deposited film are etched away during each cycle due to the reverse current of the PR plating process, which results in a smooth, stress-free film with a uniform composition as shown in Fig. 1(b). Apart from micrographs using SEM, the

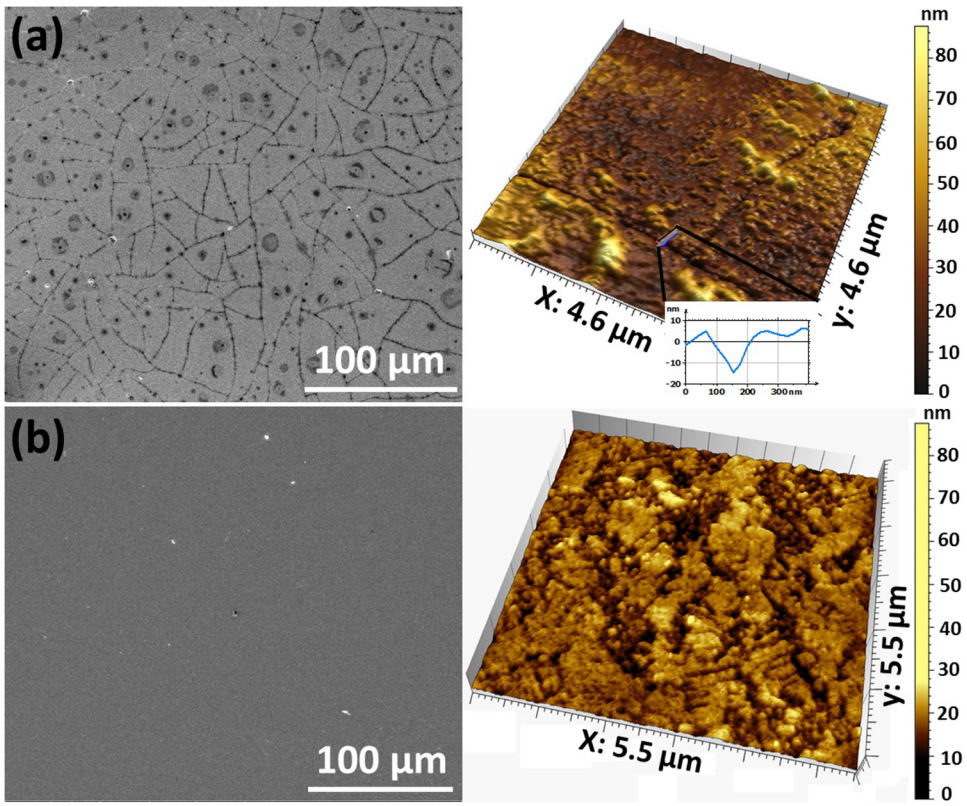


FIG. 1. Surface morphology of the films deposited at 20 mA/cm^2 density using (a) DC plating and (b) PR plating techniques. The right-hand side image for both the figures shows the corresponding AFM images. A measurement of the micro-crack depth for DC plated film is shown in the inset.

Published under license by AIP Publishing.

improvements on the surface morphology are also examined using AFM imaging as shown in Figs. 1(a) and 1(b). The RMS roughness of the DC plated film is measured to be 4.4 nm, whereas the same for the PR plated film is 3.7 nm. However, the major benefit is achieved due to the disappearance of micro-cracks from the surface topography in the PR plated film. This significant reduction in the stress of the developed film is particularly useful not only for depositing very thick films but it also improves the magnetic properties by reducing the grain size comparable to the single domain size, which is essential for magnetic MEMS applications.

The PR plating method improves the magnetic properties significantly as shown in Fig. 2. The perpendicular and parallel coercivities of the DC plated film are 41.4 kA/m (0.52 kOe) and 24 kA/m (0.30 kOe), respectively, whereas the same values for the PR deposited film are 268 kA/m (3.35 kOe) and 175 kA/m (2.19 kOe), respectively. This significant improvement in the magnetic property can be attributed to the structural uniformity of the PR plated film. The squareness factor ($S = M_R/M_S$, where M_R is the remanence magnetisation and M_S is the saturation magnetisation) of the PR electrodeposited film in the perpendicular and parallel directions are 0.3 and 0.42, respectively. The corresponding values for the DC plated films are 0.03 and 0.3, respectively.

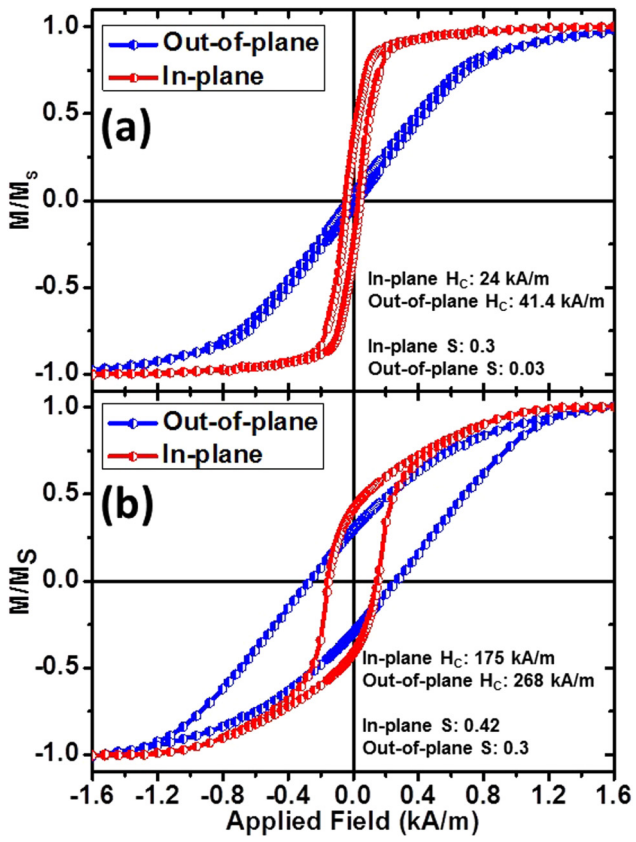


FIG. 2. Magnetic hysteresis loop measurement of the 1 h deposited films at room temperature: (a) DC plated film and (b) PR plated film. Coercivity (H_C) and squareness (S) values are mentioned for the respective loops.

B. Study of hard magnetic properties with thickness variation

The above-mentioned optimized deposition conditions are used to develop Co-rich CoPtP films with various thickness values and the corresponding crystalline structures and magnetic properties are compared in this section. The deposition rate for the PR plated films is found to be ~3 μm/h. However, the deposition rate drops slightly for long duration of plating. Initially, the deposition starts on the Cu/Ti seed layered substrate but, as the plating process progresses, the film keeps depositing on the already grown CoPtP film. This causes the loss of conductivity on the substrate and, as a result, the plating rate drops. This, however, does not affect the film composition much. The deposited films are observed to retain their composition for long deposition time. This improvement is achieved due to the addition of the stabilizing agent in the plating bath which restrains the bath from precipitating over long time. However, the pH of the bath is constantly monitored during electrodeposition. Co-rich CoPtP films with thicknesses of 0.9 μm, 2.9 μm, 6.1 μm, 12.5 μm, 20.2 μm, and 26 μm, are deposited by varying the deposition time. The films are visually smooth, shiny, and showed good adherence to the substrate. Further surface morphology imaging of the CoPtP films with various thicknesses is performed using SEM, which are shown in Fig. 3. The images suggest that while the deposited films with lower thicknesses are smooth and stress-free, micro-cracks tend to appear occasionally for high thickness film. This could be attributed to the internal stress that appears due to the increase of the film thickness. However, the effect of the stress is still less significant compared to the DC plated films as the micro-cracks for thickest PR plated film [Fig. 3(c)] is still less-dense compared to that for the much thinner DC plated film [Fig. 1(a)].

Cross-sectional HR-TEM image of the PR deposited thin (0.9 μm) and thick (26 μm) films is shown in Fig. 4, which clearly shows the nano-scale grain size of the developed films. As labeled in Fig. 4(b), the lines between the grains denote the grain boundaries. The micro-graphs and SAED images in the insets show the highly oriented crystalline nature of the developed films and both the films composed of fcc (111)/hcp (002) rings. The d-spacing value of 2.02 Å is found from the SAED rings which could be attributed to either of fcc (111) or hcp (002) phases. From the XRD analysis (Fig. 5), it is observed that a high intensity peak is obtained at 43.4° for all thickness values of the film, which also indicates that there could be the coexistence of both Co-fcc (111) and Co-hcp (002) phases. However, a small diffraction peak of Co-hcp (101) is observed at 50.5° strengthening the occurrence of the hcp phase. For thin to moderately thick films of CoPtP, the absence of hcp (100) reveals the possibility of

Published under license by AIP Publishing.

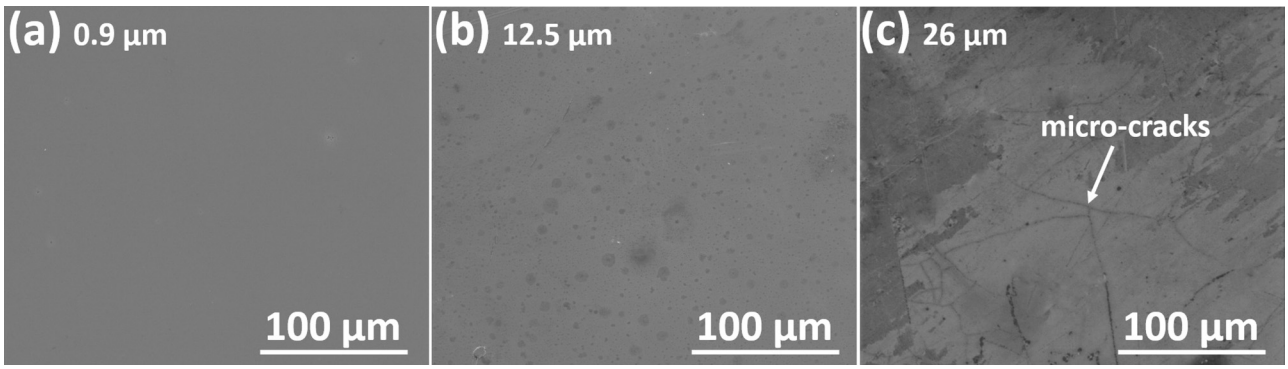


FIG. 3. Surface morphology of the PR plated CoPtP films with thicknesses: (a) 0.9 μm, (b) 12.5 μm, and (c) 26 μm.

smaller crystallites. The Co-hcp (100) peak is observed at 40.5° for a 26 μm thick film, which indicates a strong c-axis orientation of the columnar crystal structure normal to the surface plane as confirmed by the TEM image [Fig. 4(b)] as well. The grain size of the films is determined using the Scherrer equation

$$\tau = \frac{K\lambda}{\beta \cos\theta}, \tag{2}$$

where τ is the mean grain size, K is a dimensionless shape factor with a value close to unity, λ is the X-ray wavelength (1.54 Å), β is the line broadening at half the maximum intensity (FWHM), and θ is the Bragg angle (in degrees).

The in-plane and out-of-plane magnetic hysteresis loops for three different thicknesses are shown in Fig. 6. The comparison of structural and magnetic properties of CoPtP films with different thicknesses is given in Table I. The variations of the in-plane and out-of-plane H_C, S, M_R, and $(BH)_{max}$ with the thickness of the plated CoPtP films are shown in Figs. 7(a)–7(d), respectively. It is observed that both H_C and S decrease with thickness. H_C reduces due to the formation of multi-domain structure within a single grain. If the size of the grain is smaller than the domain wall thickness, it cannot consist of multiple domains separated by the domain walls. On the other hand, if the grain size exceeds the size of a single domain, multiple domains can be formed within a single grain, making them a multi-domain grain. In this case, the magnetization process is determined by domain wall pinning at the grain boundaries.[28] Theoretically, the H_C of such nano-crystalline materials is given by

$$H_C = p_c \frac{\sqrt{AK_1}}{M_S D}, \tag{3}$$

where p_c, A, K_1, M_S, and D are the particle shape pre-factor,

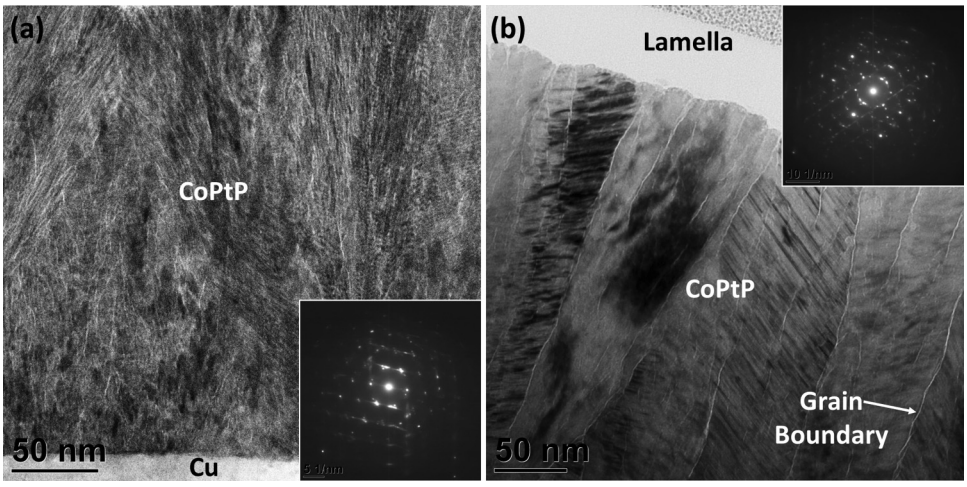


FIG. 4. Cross-sectional TEM images of the (a) 0.9 μm film and (b) 26 μm film. The insets show the SAED patterns for the respective films.

Published under license by AIP Publishing.

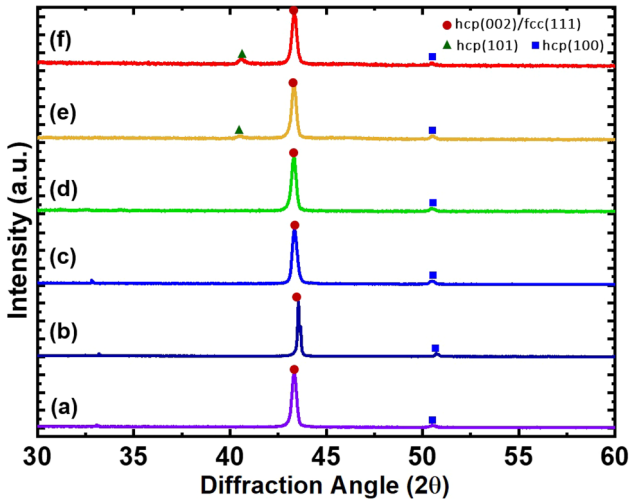


FIG. 5. X-ray diffraction patterns of Co-rich CoPtP films for different thickness values: (a) 0.9 μm, (b) 2.9 μm, (c) 6.1 μm, (d) 12.5 μm, (e) 20.2 μm, and (f) 26 μm.

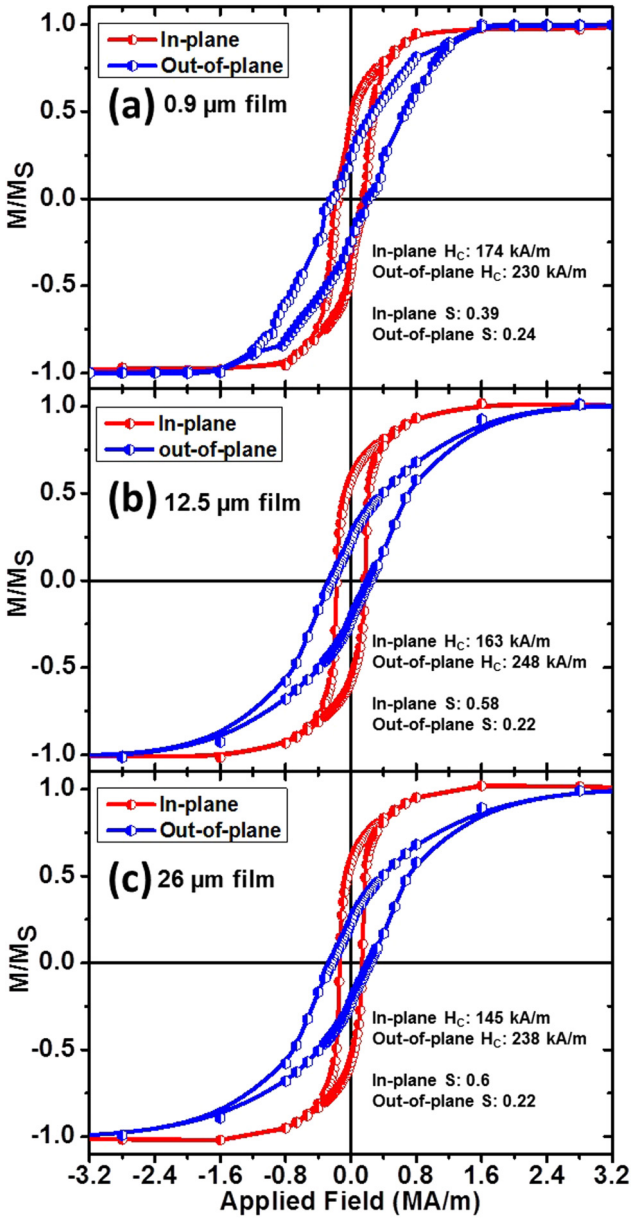


FIG. 6. Magnetic hysteresis loop measurement along parallel (in-plane) and perpendicular (out-of-plane) directions of the deposited films of thicknesses: (a) 0.9 μm, (b) 12.5 μm, and (c) 26 μm, respectively.

exchange stiffness, magneto-crystalline anisotropy, magnetization saturation, and particle diameter, respectively. From Eq. (3), it is found that as the size of multi-domain grains is increased, H_C decreases. The grain size of the deposited films is found to increase from 6.4 nm to 22.5 nm as the thickness grows from 0.9 μm to 26 μm.

The drop in coercivity can also be explained by considering the Co-hcp hard magnetic phase. Pure Co-hcp is a soft magnetic phase,[29] where the addition of Pt atoms leads to replacement of a few Co atoms in the Co-hcp unit cell. This results in an increased anisotropy of the Co-hcp phase, hence making it a hard-magnetic phase. Additionally, as mentioned before, the P atoms tend to settle at the grain boundaries and act as pinning sites preventing domain wall movement and as grain growth inhibitor. It is observed that the atomic percentage of Co increases by 6.5% as the thickness increases from 0.9 μm to 26 μm, leading to the drop of Pt and consequently in the loss of coercivity. The in-plane squareness factor increases with thickness indicating the increase of in-plane anisotropy. However, the squareness factor along the out-of-plane direction remains almost constant with varying thickness of the films.

Due to the increase in Co% in the CoPtP films with growing thickness, the total magnetic moment vis-à-vis the saturation magnetization increases. This enhancement of the saturation magnetization (M_s) together with that of the squareness factor significantly increases the remanence magnetization ($M_R = S \times M_S$) along the in-plane direction by 80%, as shown in Fig. 7(c), whereas the same along the out-of-plane direction decreases slightly.

One of the important figure-of-merits for any hard-magnetic material is the maximum energy product (BH_{max}) which is defined as the area of the largest B-H rectangle that can be constructed within the second quadrant of the B-H magnetization curve. For calculating (BH_{max}), the measured M-H loop is converted to B-H loop, the BH product is derived and the maximum value is determined. Figure 7(d) shows the variation of energy product with film thickness. The BH_{max} decreases monotonically with increasing thickness.

Published under license by AIP Publishing.

TABLE I. Comparison of structural and magnetic properties of the different films with varying thicknesses.

Film thickness (μm)	Atomic composition (%)	Grain size (nm)	Coercivity (kA/m)	
			In-plane	Out-of-plane
0.9	Co—79.4 Pt—19.5 P—1.1	6.36	174	230
2.9	Co—79.6 Pt—19.2 P—1.2	6.58	175	268
6.1	Co—80.3 Pt—18.5 P—1.2	7.08	168	263
12.5	Co—83 Pt—15.4 P—1.6	10.96	163	248
20.2	Co—85.3 Pt—12.9 P—1.8	15.03	157	239
26	Co—85.9 Pt—12 P—2.1	22.5	145	238

A maximum in-plane BH_{max} of 46 kJ/m^3 is obtained for the 0.9 μm thick film.

Further improvements in the hard-magnetic performances of PR plated Co-rich CoPtP films can be obtained by further optimizing the deposition kinetics which could lead to improved deposition rate, while maintaining the constant composition.

C. Study of switching behavior in Co rich CoPtP films

In order to understand the magnetization switching process, film thicknesses of 0.9, 2.9, and 26 μm are subjected to isothermal remanence measurements (IRMs) and dc demagnetization (DCD) measurements along the in-plane direction. The IRM measures the remanence magnetization as a function of an increasing magnetizing field starting from a random demagnetized state. In the case of DCD measurements, the films are first saturated to a large positive field. Subsequently, a small negative field is applied, then removed, and remanence magnetization is measured. The process is repeated for increasing negative fields. The IRM and DCD plots for the CoPtP films are shown in Figs. 8(a)–8(c), respectively. The corresponding magnetizations are differentiated w.r.t. the applied field and plotted in the respective insets. The IRM curves for the films show stable character with nearly zero values at the smaller applied field range and then increase gradually before saturating at large applied fields. The nature of variation for IRM plots suggests that domain nucleation and coherent rotations are responsible for magnetization reversal in the CoPtP films. The DCD curve for the thicker (26 μm) film crosses the zero point at a relatively higher field than that for the thinner films, which could be

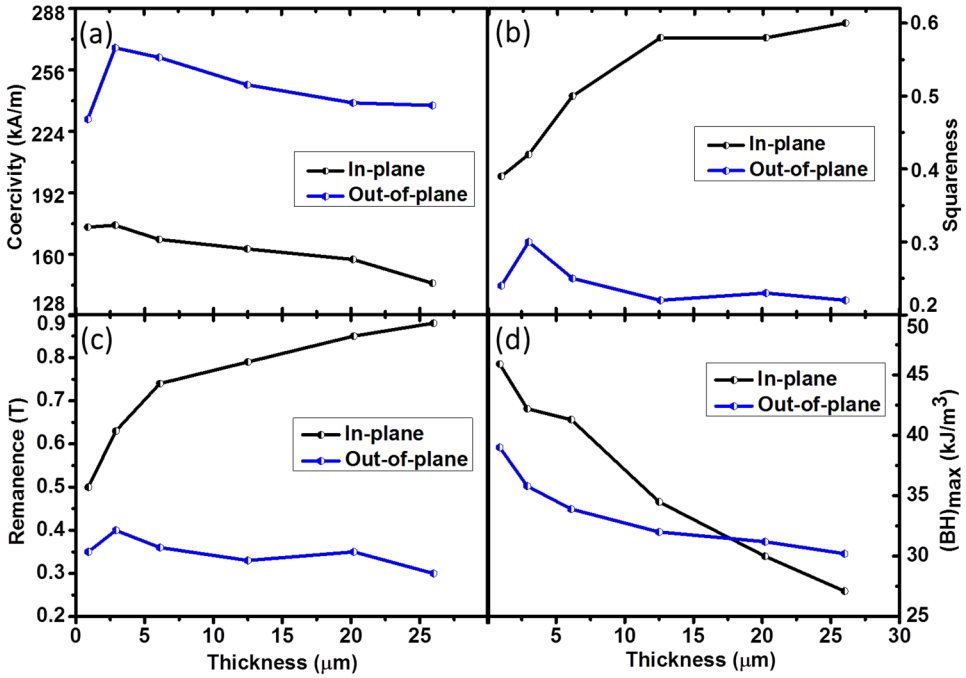


FIG. 7. Variation of hard magnetic properties, such as (a) coercivity, (b) squareness, (c) remanence magnetization, and (d) energy product (BH_{max}) for increasing film thickness is shown here.

Published under license by AIP Publishing.

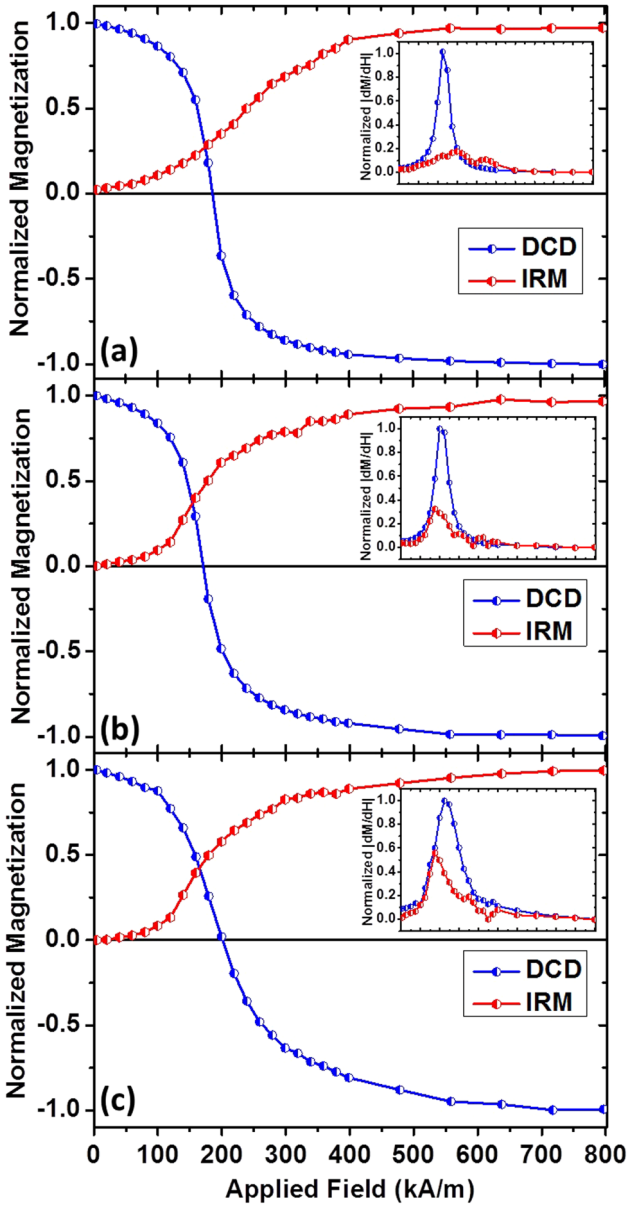


FIG. 8. The isothermal remanence (IRM) and dc demagnetization (DCD) plots for (a) 0.9 μm (b) 2.9 μm, and (c) 26 μm thick CoPtP films. The differentials (∂m/∂H) of the IRM and DCD magnetizations are plotted in the insets.

due to the increase of grain size way above the single domain size[30] for Co hcp phase leading to the higher intra-granular exchange interaction. This has been further explained later.

Also, magnetic interactions between the film grains can be established from the above measurements. Figure 9(a) shows the variation of normalized DCD against the normalized IRM characterization for the films with afore-mentioned thicknesses to decipher the magnetic interaction between the grains. For non-interacting single domain particles, the dependence of the two remanence curves should be approximately linear [represented by the dashed lines in Fig. 9(a)] according to the Stoner-Wohlfarth model,[31] following the relationship $m_d = (1 - 2m_r)$. Here, m_r and m_d are the normalized IRM and DCD remanences, respectively. Deviation from the linearity can be attributed to either exchange (positive) or dipolar (negative) interaction. The 26 μm thick film maintains the criterion of $m_d > (1 - 2m_r)$, which suggests that the main inter-granular interaction is due to ferromagnetic exchange coupling. An early peak in the derivative of IRM curve compared to that in the DCD curve [Fig. 8(c) inset] also suggests that changes in IRM occur faster which indicate positive interactions, promoting the magnetized states in the thick film. Similar nature is observed for the derivatives of IRM and DCD of the 2.9 μm film. The dominant interaction in the 0.9 μm film is dipolar in nature as $m_d < (1 - 2m_r)$ condition is fulfilled which can be seen in Fig. 8(a). The nature of strength of magnetic interactions can be further examined by using the Kelly-Henkel plot (Δm plot),[32,33] which is defined by the relation

$$\Delta m = m_d - (1 - 2m_r), \tag{4}$$

where m_r and m_d are the normalized IRM and DCD remanences, respectively. The ideal non-interacting particles are characterized by $\Delta m = 0$, whereas positive and negative peak values represent intra-grain exchange interaction and inter-grain dipolar interaction, respectively. Figure 9(b) depicts Δm as a function of the applied field. The strength of the positive peak for 26 μm thick film is higher compared to that in the 2.9 μm film. This could be attributed to the grain sizes of the corresponding films. As mentioned earlier, the grain sizes for 2.9 and 26 μm thick films are calculated to be 6.6 nm and 22.5 nm, respectively, whereas the single domain size for the Co hcp phase (dominant in all the films) is ~10 nm.[30] For the thicker film, the formation of the multi-domain structure enhances the exchange interaction. The negative peak at larger field for the 2.9 μm film could be caused due to the demagnetization field of the grains.[34] For the thinner 0.9 μm film, the inter-granular interaction is dipolar in nature. The grains for the corresponding films are randomly oriented with needle like shape as observed from the TEM image [Fig. 4(a)], which could be the reason for such interaction.

Through the magnetic and structural analysis provided so far, we can conclude that thick magnetic structures with specific nano-meter sized (comparable to single domain size) crystallites can be developed using the optimized PR deposition method which would be ideal for magnetic MEMS applications. In Sec. IV, we discuss the performance enhancement of such devices from the design point of view.

IV. PATTERNED MICRO-MAGNET DEVELOPMENT FOR MAGNETIC MEMS APPLICATIONS

In a number of integrated magnetic MEMS applications such as sensors,[35,36] actuators,[37] energy harvesting,[38–42]

Published under license by AIP Publishing.

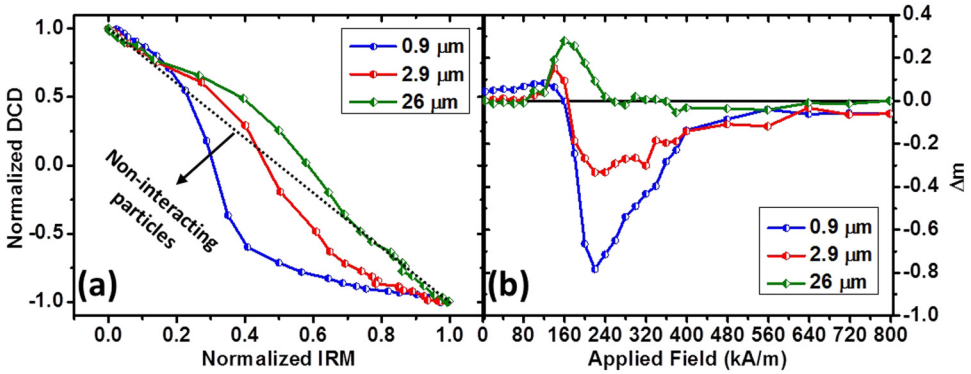


FIG. 9. (a) DCD vs IRM plot for 0.9 μm, 2.9 μm, and 26 μm thick CoPtP films. (b) Kelly-Henkel (Δm plot) for the three films, respectively.

microfluidics,[43–45] etc., permanent magnets are used as the source of magnetic field. The usage of magnetic force for different MEMS application is advantageous due to the fact that no external power is required as in the case of piezoelectricity or electrostatics. As already mentioned in the Introduction section, CMOS compatible development of high energy product (BH_{max}) permanent magnets with thickness of the order of microns to hundreds of microns is a key challenge. However, the challenge extends beyond the development of the nano-structured, high energy product magnetic material and relates to the lack of intelligent design strategies. The magnetic flux in a permanent magnet is decided by the length between its poles. The magnetic flux density diminishes due to the demagnetization field, which acts to demagnetize the magnet in a direction opposite to the direction of the magnetization.[46] As a result, the stray magnetic field appears only from the edges of the magnet when a relatively thin film/block of permanent magnet is used as the source of magnetic field in a MEMS device and a large part of the magnetic material is wasted, affecting the performance of integrated magnetic MEMS actuators/transducers. In this section, we propose a novel design strategy through micro-patterning for improving the performance of such magnetic MEMS devices using the material property obtained from the magnetic measurements of PR plated CoPtP hard magnets. Finally, different micro-patterns of CoPtP are fabricated as a combination of optical lithography and PR plating techniques which will be suitable for potential MEMS based applications.

We propose to replace a block of permanent magnet by micro-patterned array of magnets, diminishing the demagnetization effect and enhancing the magnetic stray field. In this case, the magnetic flux density can be intensified over a small space due to increase of the edges of magnetic elements, which is shown quantitatively in Fig. 10 using FEM simulation in COMSOL Multi Physics solver. In the simulation, the total volumes of the whole block and square magnetic array (including the interspace) are kept the same. For the block, a $1 \times 1\,mm^2$ structure is assumed, while the thickness is kept fixed at 10 μm for all the simulations. In the case of the patterned structure, $50 \times 50\,\mu m^2$ square shaped structures are considered while the inter-space between successive patterned elements is assumed to be 50 μm as well. We assumed ideal permanent magnets in all the simulations with uniform magnetization throughout the structures and the magnetization direction is perpendicular to the plane of the magnet. As for the material, we have taken CoPtP permanent magnets having coercivity (H_C) and remanent magnetic induction (B_R) values of 268 kA/m and 0.4 T which are in accordance with the results obtained in Sec. III B. It is observed that the stray field that appears is only from the edge of the magnets, which validates the afore-mentioned theory. The scale bar is kept same for both whole block and patterned magnets for even comparison. While the largest magnetic flux density appears at the edge region, which is about 0.4 mT, it is reduced almost to zero in other regions. The magnetic flux density along a line through the middle of the magnetic structures on the surface of the magnets is also compared in Fig. 10. For the block magnet, the maximum field is observed exactly above the edge of the block magnets whereas the field reduces to zero elsewhere. In the case of the patterned magnet, this peak is observed at each edge of the patterned structure periodically. The average magnetic flux density on the surface is found to be 0.03 mT for the block magnet which dramatically increases to 0.15 mT for the micro-patterned case showing the potential of micro-patterned magnets as a source of magnetic field in a range of MEMS applications. Different micro-patterns of CoPtP permanent magnets are fabricated using a combination of optical lithography and PR plating techniques. The process to develop micro-patterned CoPtP magnets starts by cleaning a blank silicon wafer in acetone, isopropyl alcohol, and DI water. Then a Ti/Cu (20/200 nm) seed layer is sputtered on the wafer. The AZ9260 positive photoresist is spun on the wafer and a 20 μm thick resist layer is developed using optimized double spinning process. After developing the resist, the wafer is diced into four equal pieces and CoPtP is electrodeposited in one of the pieces in a beaker containing 200 ml of the electrolytic bath using the PR plating technique with the optimized deposition parameters described in

Published under license by AIP Publishing.

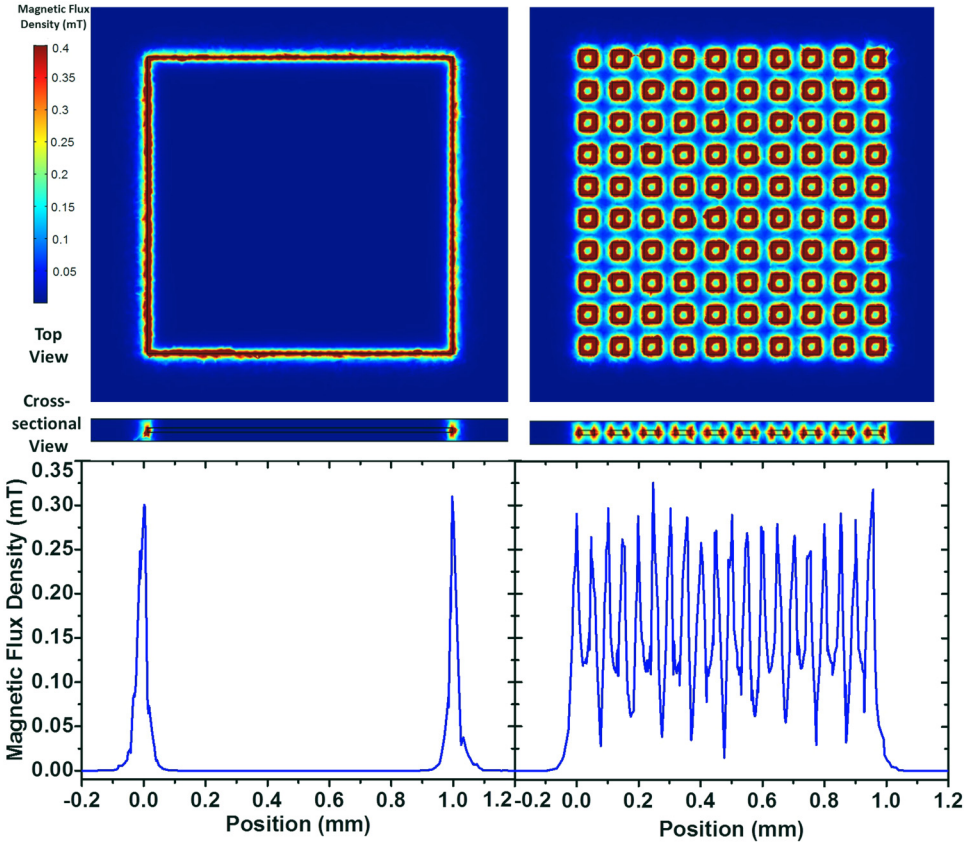


FIG. 10. FEM simulation using COMSOL to show the advantage of using micro-patterns (right) compared to a block (left) of integrated permanent magnet, minimizing the demagnetization field. Both top view (on surface of the magnets) and cross-sectional view are shown. Plots below show the variation of magnetic flux density along a line through the middle of the magnetic structures.

Sec. III A. The SEM images of the developed micro-patterned structures with a thickness of ~10 μm are shown in Fig. 11 confirming the high shape accuracy obtainable from the micro-fabrication process. Since the pH of the bath is 8, which is basic, it acts as a stripper for the photoresist. It is observed that the resist profile is not maintained after long plating durations. Hence, in a future optimization of the process, either the mask (a bright-field mask could be used for the same resist) or an alternative resist could be used for developing thicker patterns of the CoPtP permanent magnets which could be potentially integrated in future magnetic MEMS devices.

Extending our analysis using FEM simulations, the magnetic flux density maps at an observation height of 10 μm for different square pattern structures for varying pattern heights/thicknesses and pattern inter-spacing distances/gaps are shown in Fig. 12. For smaller inter-spacing distance (10 μm) [Fig. 12(a)], the magnetostatic interaction between successive pattern elements is very strong and significantly deteriorates the stray field from the entire structure except at the edges. Therefore, the patterned structures with smaller inter-spacing gaps behave like block magnet as in the previous case. From Fig. 12(a), we observe that the magnetic flux density intensifies at the outer edges with an increase of pattern height due to the increase in the magnetic volume. However, the inter-spacing gap has stronger impact on the overall magnetic flux density [Fig. 12(b)]. As the gap is increased from 10 to 100 μm, the edge effect from the individual pattern elements comes into play. At large gaps, the patterns behave like individual elements as there is almost no contribution from neighboring magnetic elements and regions of zero flux density are observed in between the patterns.

To understand the effect of different parameters of the patterned structures, such as length/width/diameter, height, inter-spacing distance, and shape, detailed FEM simulations have been performed. We have considered square and circular patterned structures. The side lengths of the squares and the diameter of the circles are assumed to be 50 μm while the height of the patterns (or effectively the aspect ratio) is varied. The average magnetic flux density (B_a) is calculated at

Published under license by AIP Publishing.

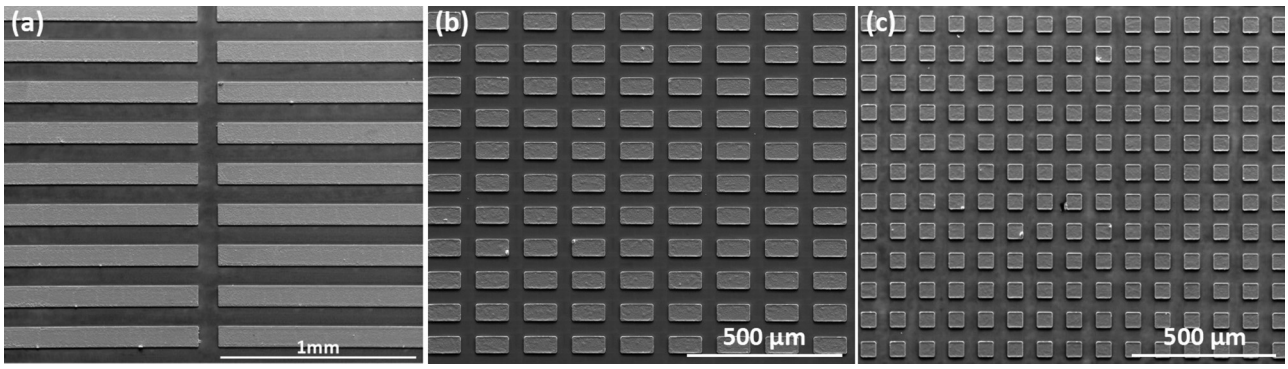


FIG. 11. Micro-fabricated patterned structures of the CoPtP magnetic material (a) 2500 × 50 μm^2 stripes, (b) 100 × 50 μm^2 rectangles, and (c) 50 × 50 μm^2 squares. Each pattern has a thickness of ~10 μm.

10 μm [Figs. 13(a) and 13(b)], 30 μm [Figs. 13(c) and 13(d)], and 50 μm [Figs. 13(e) and 13(f)] distances above the magnet surfaces. It is to be noted that magnetic properties are dependent on the thickness and varies with it. However, we have considered same magnetic parameters for all our simulation for simplicity of the analysis. Also, the feature sizes of each pattern elements and separation between them are large enough to avoid any nano-scale interactions such as inter-element exchange coupling and dipolar interaction. In order to calculate the magnetic flux density in COMSOL, a plane is defined at the desired heights and surface average is calculated which determines the average magnetic field over the entire plane at this height. For all the simulations, the total area (including the gaps between successive patterned structures) is kept fixed to 1 mm^2. The simulation results are shown in Fig. 13. The average magnetic field variation for non-patterned/continuous block structure is also included in each plot as a reference. The corresponding inset figures show the variation of B_a for variation of inter-pattern spacing distances for different aspect ratios (ARs = width/height). In all cases, B_a increases as the pattern height is increased due to increase of total magnetic volume. In coherence with the previous figure, the separation gap between the patterns plays more prominent role in the design. At lower observation height (10 μm), the stray field is much stronger and is the main area of interest. Here, the maximum B_a is generated for the 50 μm inter-spacing gap, which is equal to the feature size of the patterns, for most of the pattern heights (or alternatively for most ARs). The B_a value drops on either increase or decrease of the inter-spacing gaps. This can be explained using the magnetic flux mapping of Fig. 12(b).

At 50 μm gap, the edge effect of the individual pattern elements is shown, whereas there is still some overlap between the stray field from neighboring patterns which lifts the B_a value. As the gap is increased, there are regions of no flux density between successive patterns which reduces the B_a. For smaller gaps, the only significant flux arises from the outer edges only with almost no flux from the inner regions reducing the B_a value. At 30 μm observation height, the overlapping field distributions are too weak to reach. The more intense fields from the edges of the patterns with larger inter-spacing play a crucial role there and maximum B_a is observed for higher inter-spacing values. With further increase of observation height (50 μm), the patterns with the lowest inter-spacing show the highest B_a. In this case, most stray fields are too feeble to reach such an observation height. Possibly, the only contributing factor here is the uninterrupted fields from the extreme outer edges of the magnetic structures. At higher observation heights, the inter-spacing gap plays a less significant role as B_a does not change noticeably for any of the ARs which is indicated in the insets of Fig. 13. It is to be mentioned here that the volume of the total magnetic material is being compromised as a result of the micro-patterning. In order to maintain the same magnetic volume while laterally patterning the film/block, the height of the individual pattern would have to be increased. In some cases, this would become unrealistic to realize in practice using conventional deposition methods like electroplating. Hence, we have kept the thickness of all the magnetic structures same to develop a simple model while compromising on the magnetic volume. However, the advantage of micro-patterning is still clear from our analysis.

Thus, it can be concluded that for many magnetic field based MEMS devices, micro-patterning provides significant advantages over a simple film/block of the magnet and most of these advantages can be availed by keeping the target object (micro-coil for magnetic actuators/transducers[35–42]) close to the patterned permanent magnets. In many other applications, field uniformity is important (such as in the case of microfluidics,[43–45] where magnetic particles may get inadvertently trapped at each micro-magnet site). In such cases also, the micro-patterning provides significant advantages over the film/block of the magnet by maintaining uniform field distribution over a relatively large area. At lower observation height, the maximum flux density is obtained for patterns where the inter-spacing gap is comparable to the corresponding

Published under license by AIP Publishing.

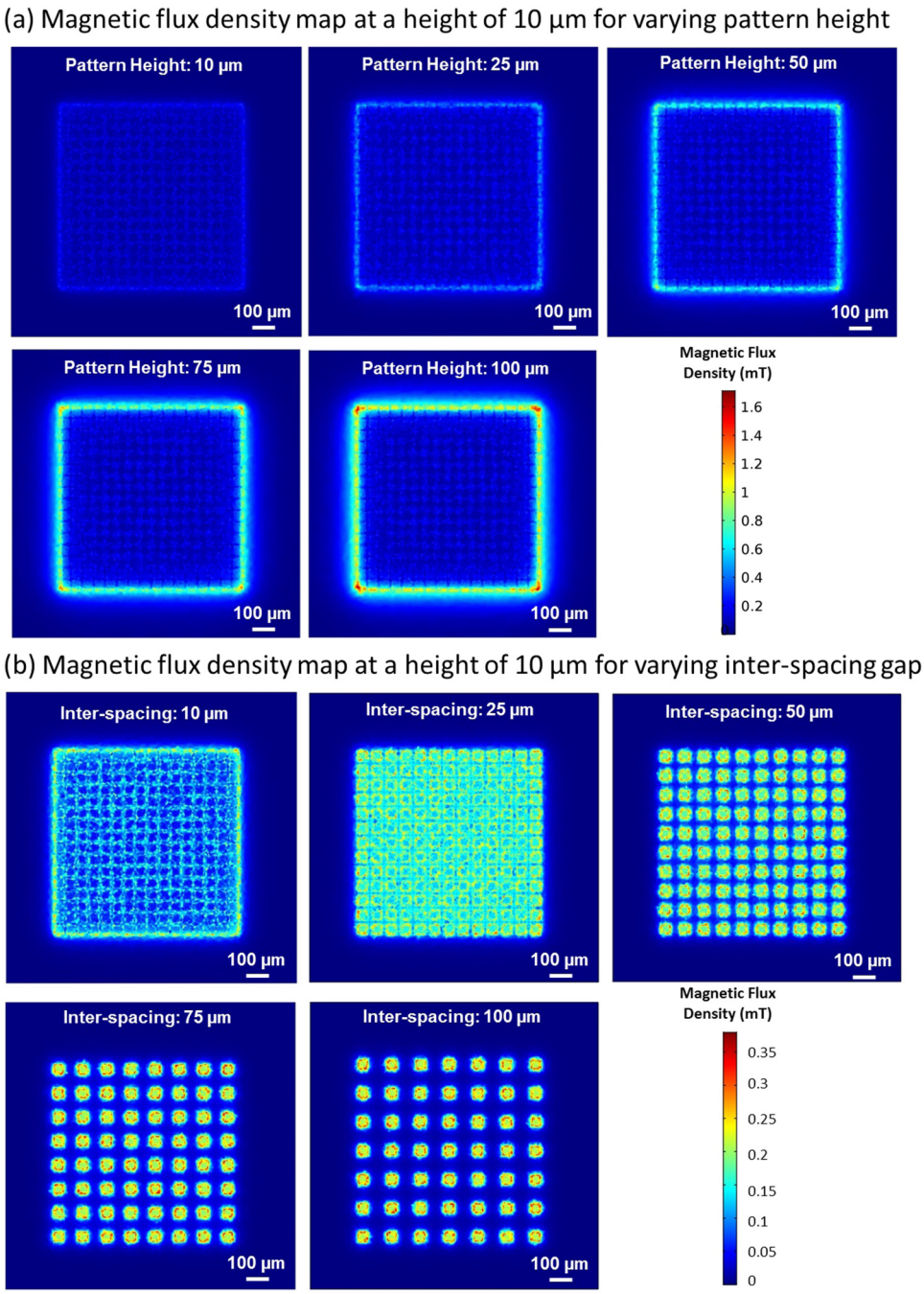


FIG. 12. Variation of the average magnetic field with pattern heights observed at a distance of 10 μm above the surface of the patterned structures for different inter-pattern gap values which are obtained using COMSOL Multiphysics simulations.

pattern feature sizes. The flux density changes in a complicated manner with an increase in the observation height. One point to be mentioned is that we have considered ideal micro-magnets with perfect conditions and geometries which may not occur for fabricated micro-magnet structures. Therefore, it would be ideal to experimentally measure the stray field from micro-magnets which is, however, out of scope of this work. Such measurements along with the complete integration

Published under license by AIP Publishing.

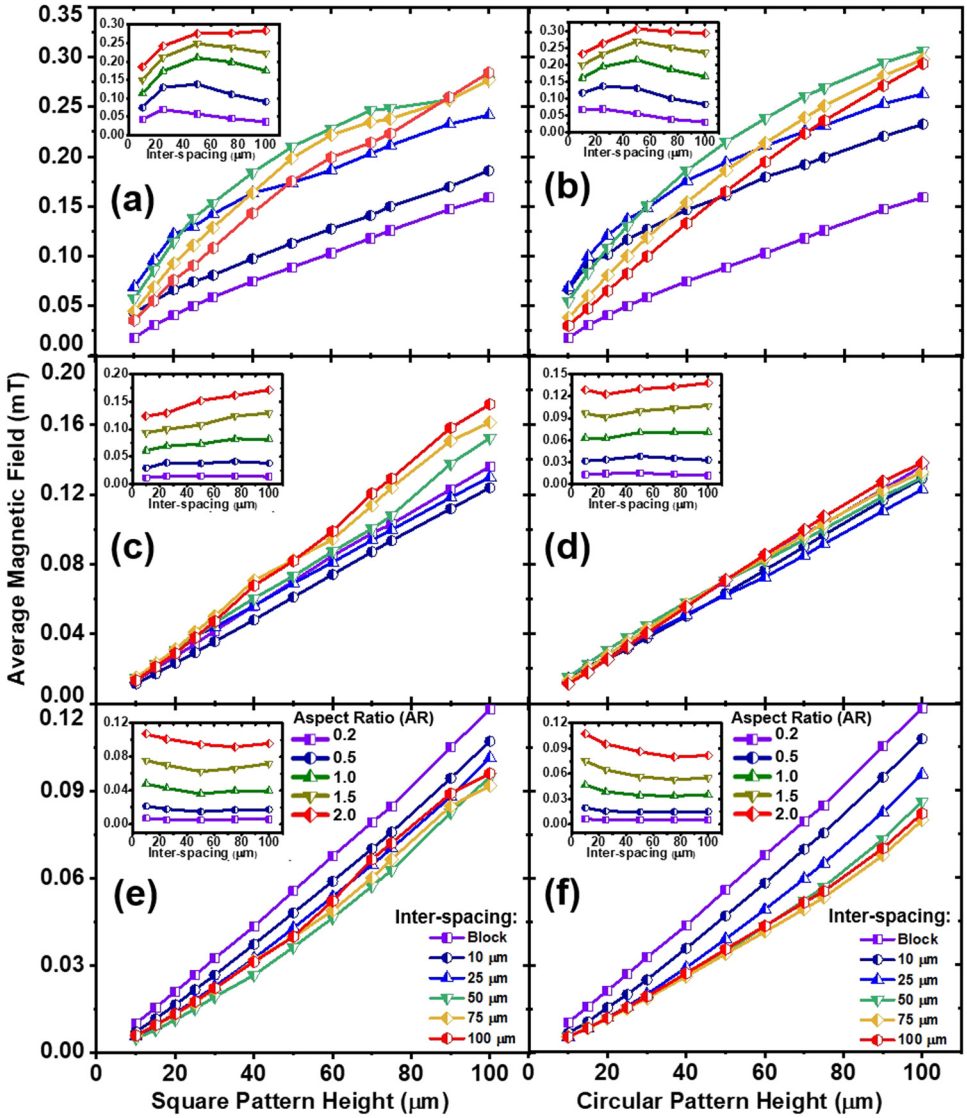


FIG. 13. Variation of the average magnetic field with pattern heights observed at a distance of [(a) and (b)] 10 μm, [(c) and (d)] 30 μm, and [(e) and (f)] 50 μm above the surface of the magnetic structures for different inter-pattern gap values. The same for the continuous block of magnet is also shown in each plot as a reference. The inset shows the variation of average magnetic field as a function of inter-spacing distances of the patterns with different aspect ratios (ARs).

of the MEMS device incorporating the developed thick magnetic structures with optimized nano-crystallites, where the design is underpinned by the analysis provided in this section, can be attributed to the future work.

V. CONCLUSION

We have developed and characterized the structural and magnetic properties of Co-rich CoPtP films electrodeposited using optimized Pulse Reverse (PR) technique. By using a combination of forward and reverse pulse times during deposition, the film stress is reduced significantly, which results in smooth, crack-free films of thickness up to 26 μm. The deposited film of thickness ~3 μm shows a coercivity of 268 kA/m, a remanence of 0.4 T, and a maximum energy product of 35 kJ/m^3 in the out-of-plane direction. As the thickness is increased up to 26 μm, the coercivity reduces due to the increase of grain size and the Co content in the alloy structure. The in-plane squareness factor increases by 1.5 times as the thickness is increased, which results in an enhancement of the in-plane

Published under license by AIP Publishing.

remanence value. However, the variation in the hard magnetic property due to the change of thickness is not significant, which could be due to the unchanged atomic composition and crystalline structure leveraged by the stabilization of the electrolytic bath. The magnetization reversal behavior of the deposited films indicates that the nature of magnetic interaction is significantly influenced by the thickness of the films. The dipolar interaction for the thinner films changes to exchange coupling at a higher thickness due to the increase of grain size.

We also proposed an innovative design strategy to integrate CoPtP in magnetic MEMS devices by micro-patterning and analyzed the same using the finite element method. The demagnetization fields of the magnetic elements are minimized through optimized micro-patterned structures which improve the viability of PR deposited CoPtP micro-magnets in potential MEMS based applications.

ACKNOWLEDGMENTS

This work is financially supported by a research grant "CONNECT" from the Science Foundation Ireland (SFI) and is co-funded under the European Regional Development Fund (Grant No. 13/RC/2077). This is also partly funded by the EU-H-2020 project "Enables", Project ID: 730957. This work is financially supported by the Irish Research Council (Project No. GOIPD/2016/474). The authors would like to thank Dr. Michael Schmidt for performing the TEM imaging.

REFERENCES

[1]S. N. Piramanayagam, J. Appl. Phys. **102**, 2 (2007).
[2]G. Ju, Y. Peng, E. K. Chang, Y. Ding, A. Q. Wu, X. Zhu, and Z. Fan, IEEE Trans. Magn. **51**(11), 1–9 (2015).
[3]D. P. Arnold and N. Wang, J. Microelectromechanical Syst. **18**, 1255–1266 (2009).
[4]D. Niarchos, Sens. Actuators A Phys. **109**, 166–173 (2003).
[5]R. Skomski, P. Manchanda, P. Kumar, B. Balamurugan, A. Kashyap, and D. J. Sellmyer, IEEE Trans. Magn. **49**, 3215–3220 (2013).
[6]N. Wang, B. J. Bowers, and D. P. Arnold, J. Appl. Phys. **103**, 07E109 (2008).
[7]L. K. Lagorce, O. Brand, and M. G. Allen, J. Microelectromechanical Syst. **8**, 2–9 (1999).
[8]T. Shima, K. Takanashi, Y. K. Takahshi, and K. Hono, Appl. Phys. Lett. **85**, 2571–2573 (2004).
[9]H. Yamane, K. Takeda, and M. Kobayashi, Appl. Phys. Lett. **106**, 052409 (2015).
[10]H. An, Q. Xie, J. Wang, T. Sannomiya, S. Muraishi, Z. Zhang, Y. Nakamura, and J. Shi, J. Vac. Sci. Technol. A **33**, 021512 (2015).
[11]G. Varvaro, E. Agostinelli, S. Laureti, A. M. Testa, J. M. Garcia-Martin, F. Briones, and D. Fiorani, J. Phys. D Appl. Phys. **41**, 134017 (2008).
[12]B. Varghese, S. N. Piramanayagam, Y. Yang, S. K. Wong, H. K. Tan, W. K. Lee, and I. Okamoto, J. Appl. Phys. **115**, 17B707 (2014).
[13]F. M. F. Rhen and J. M. D. Coey, J. Magn. Magn. Mater. **322**, 1572–1575 (2010).
[14]F. M. F. Rhen, E. Backen, and J. M. D. Coey, J. Appl. Phys. **97**, 113908 (2005).
[15]O. D. Oniku, B. Qi, and D. P. Arnold, J. Appl. Phys. **115**, 17E521 (2014).
[16]S. Kulkarni and S. Roy, J. Appl. Phys. **101.9**, 09K524 (2007).
[17]S. Guan and B. J. Nelson, J. Magn. Magn. Mater. **292**, 49–58 (2005).
[18]L. Callegaro, E. Puppin, P. L. Cavallotti, and G. Zangari, J. Magn. Magn. Mater. **155**, 190–192 (1996).
[19]L. Vieux-Rochaz, C. Dieppedale, B. Desloges, D. Gamet, C. Barragatti, H. Rostaing, and J. Meunier-Carus, J. Micromechanical Microeng. **16**, 219–224 (2006).
[20]T. S. Ramulu, R. Venu, S. Anandakumar, V. Sudha Rani, S. S. Yoon, and C. G. Kim, Thin Solid Films **520**, 5508–5511 (2012).
[21]N. Wang and D. P. Arnold, IEEE Trans. Magn. **44**, 3969–3972 (2008).
[22]S. Kulkarni and S. Roy, J. Magn. Magn. Mater. **322**, 1592–1596 (2010).
[23]R. J. Morrissey and H. Kroll, U.S. patent 4,673,472 (16 June 1987).
[24]J. Zhang, S. Agramunt-Puig, N. Del-Valle, C. Navau, M. D. Baro, S. Estrade, F. Peiro, S. Pane, B. J. Nelson, A. Sanchez, J. Nogues, E. Pellicer, and J. Sort, ACS Appl. Mater. Interfaces **8**, 4109–4117 (2016).
[25]J. Zhang, S. Pané, J. Sort, and E. Pellicer, Adv. Mater. Interfaces **3**, 1600336 (2016).
[26]O. D. Oniku and O. D. P. Arnold, ECS Trans. **50**, 167–174 (2013).
[27]S. Roy, A. Connell, M. Ludwig, N. Wang, T. O'Donnell, M. Brunet, P. McCloskey, C. ÓMathúna, A. Barman, and R. J. Hicken, J. Magn. Magn. Mater. **290-291**, 1524–1527 (2005).
[28]G. Herzer, IEEE Trans. Magn. **26**, 1397–1402 (1990).
[29]S. Sun and C. B. Murray, J. Appl. Phys. **85**, 4325–4330 (1999).
[30]A. Butera, J. L. Weston, and J. A. Barnard, J. Appl. Phys. **81**, 7432–7436 (1997).
[31]H. W. Zhang, C. B. Rong, X. B. Du, J. Zhang, S. Y. Zhang, and B. G. Shen, Appl. Phys. Lett. **82**, 4098–4100 (2003).
[32]A. Harres, R. Cichelero, L. G. Pereira, J. E. Schmidt, and J. Geshev, J. Appl. Phys. **114**, 043902 (2013).
[33]B. Jiang, D.-S. Yang, A. N. Ulyanov, and S.-C. Yu, J. Appl. Phys. **95**, 7115–7117 (2004).
[34]A. Lisfi, S. Pokharel, O. Akioya, N. H. Alqhtany, and M. Wutting, AIP Adv. **7**, 056206 (2017).
[35]D. W. Lee, M. Eissa, A. Gabrys, B. Shulver, E. Mazotti, S. Lavangkul, S. Chevacharoenkul, N. Murphy, F. Wang, Y. Zhang, and W. French, IEEE Trans. Magn. **53**, 1–4 (2017).
[36]D. Rühmer, F. Ludwig, and M. Schilling, Sens. Actuators A Phys. **238**, 229–233 (2016).
[37]J. J. Zárate, G. Tosolini, S. Petroni, M. De Vittorio, and H. Shea, Sens. Actuators A Phys. **234**, 57–64 (2015).
[38]D. Mallick, A. Amann, and S. Roy, J. Microelectromechanical Syst. **26**, 273–282 (2016).
[39]M. Han, Q. Yuan, X. Sun, and H. Zhang, J. Microelectromechanical Syst. **23**, 204–212 (2014).
[40]Q. Zhang and E. S. Kim, J. Microelectromechanical Syst. **24**, 384–394 (2015).
[41]D. Mallick, A. Amann, and S. Roy, Phys. Rev. Lett. **119**, 197701 (2016).
[42]P. Podder, D. Mallick, A. Amann, and S. Roy, Sci. Rep. **6**, 37292 (2016).
[43]Y. Y. Huang, P. Chen, C. H. Wu, K. Hoshino, K. Sokolov, N. Lane, and J. X. Zhang, Sci. Rep. **5**, 16047 (2015).
[44]P. Tseng, J. Lin, K. Owsley, J. Kong, A. Kunze, C. Murray, and D. Di Carlo, Adv. Mater. **27**, 1083–1089 (2015).
[45]O. Osman, S. Toru, F. Dumas-Bouchiat, N. M. Dempsey, N. Haddour, L. F. Zanini, F. Buret, G. Reyne, and M. Frenea-Robin, Biomicrofluidics **7**, 054115 (2013).
[46]R. Skomski and J. M. D. Coey, Scr. Materialia **112**, 3–8 (2016).

Published under license by AIP Publishing.